# 7

# Tuning Range Extension of an Oscillator Through CM Resonance

In this chapter, we introduce a method to broaden a tuning range of a CMOS LC-tank oscillator without sacrificing its area. The extra tuning range is achieved by forcing a strongly coupled transformer-based tank into a common-mode resonance at a much higher frequency than in its main differential-mode oscillation. The oscillator employs separate active circuits to excite each mode but it shares the same tank, which largely dominates the core area but is on par with similar single-core designs. The tank is forced in common-mode oscillation by two injection locked Colpitts oscillators at the transformer's primary winding, while a two-port structure provides differential-mode oscillation. An analysis is also presented to compare the phase noise performance of the dual core oscillator in common-mode and differential-mode excitations. A prototype implemented in digital 40 nm CMOS verifies the dual mode oscillation and occupies only 0.12 $mm^2$ and measures 56% tuning range.

## 7.1 Introduction

Oscillator design for multi-mode multi-band (e.g., Fourth or Fifth Generation (4G/5G) cellular) applications demands wide tuning range (TR) while ensuring sufficiently low phase noise (PN) for a range of targeted frequency bands. The maximum achievable TR of a traditional single-core LC-tank oscillator is limited at 35%–40% by a $C_{\rm on}/C_{\rm off}$ capacitance tuning ratio of its switched-capacitor network, further constrained by large size of its switches needed to prevent deterioration of the LC tank's quality (Q)-factor. For example, the Q-factor of a switched-capacitor network in a 40 nm technology is about

80 at 4 GHz resonant frequency when $C_{\text{on}}/C_{\text{off}} = 2$. For an inductor's Q-factor of 15 at this frequency, the tank's equivalent Q-factor reduces to 12.6.

The most straightforward solution seems to be designing two *separate* oscillators [1,2] at the expense of large area, and the need for high-frequency source-selecting multiplexers, which increase power consumption and noise floor. A system-level local oscillator (LO) solution in [3] uses a single 40-GHz oscillator followed by a $\div 2$ divider and an LC-tank mixer to generate 20 and 30 GHz LO signals. However, the extra mixer costs significant power and area as well as it produces spurs. Another attempt is to decrease the area of a *two-core* oscillator by placing one inductor underneath the other [4, 5]. However, the top inductor has to be very large so that the other one can be placed at its center without degrading the top inductor's quality factor. Therefore, the oscillator area is still considerably larger than that of a single-tank oscillator.

Employing switched resonator tanks, in which the tank's inductance is controlled by turning on/off interconnecting switches, is another TR expanding technique [6–13]. However, the switches' resistance limits the tank's Q-factor, thus degrading the oscillator PN [14]. Transformer-based dual-band oscillators [15, 16] offer wide but not continuous tuning range. A switched-shielded transformer [17] is another method to increase the oscillator's tuning range but it appears effective only at mm-wave frequencies. A shielded inductor [18] with a shorting switch is inserted between two windings of a transformer [17]. The coupling factor between the windings changes as to whether the current is flowing in the shielded inductor or not. This transformer is not large; however, its inductors' quality factor gets compromised. Consequently, this range-increasing technique is interesting for mm-wave applications where the tank's quality factor is rather limited by the capacitive part; however, for the single-GHz RF frequencies, the degradation of the tank's Q-factor would seem to be excessive.

Recent works on mode-switching oscillators significantly improve the PN versus TR trade-off [19–21]; however, they *do not* improve the TR versus die area trade-off. For example, Li et al. [20] switches between resonant modes (even/odd) of two capacitively and magnetically coupled LC resonators, as shown in Figure 7.1(a). Strong magnetic coupling enhances the difference between the two resonant frequencies; hence, a continuous TR extension calls for a low coupling factor, such that the transformer ends up to be quite large. Unfortunately, the recent CMOS technology nodes (28 nm and, to a lesser extent, 40 nm) have brought about very tough minimum metal-density

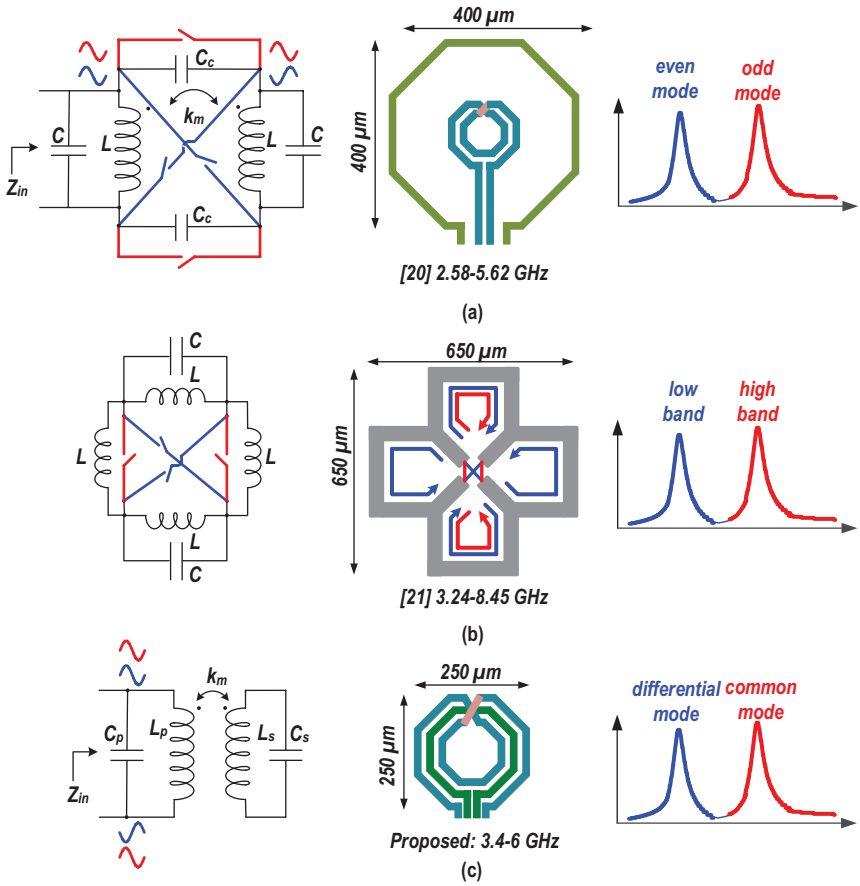


**Figure 7.1** LC tanks for wide tuning range: (a) resonant mode switching technique [20]; (b) band switching technique [21]; (c) introduced technique in [33, 34].

requirements; therefore, the inductors and transformers should be filled with a lot of dummy metal pieces [22]. This has negative consequences on inductors as resistive losses due to eddy currents in the dummy fills degrade the Q-factor. And, that is in addition to increasing the parasitic capacitance, thus narrowing the TR. The losses are even more severe in the weakly coupled transformers. The spacing between their primary and secondary windings is larger (see Figure 7.1(a)) and must be filled with dummy metal pieces, but it is precisely where the magnetic flux is concentrated the most.

In [21], as shown in Figure 7.1(b), four identical inductors are coupled through four mode-switching transistors, providing two oscillation bands. In a *low-band* oscillation mode, there is no AC current flow possibility in two

of these inductors (see Figure 7.1(b)); however, in a *high-band* mode, the AC current can flow in all the inductors. Thus, the effective inductance value in each band could be controlled. Obviously, the four inductors significantly increase the area.

Considering that not all applications require as stringent PN performance as does cellular wireless, we concentrate in this chapter on maintaining the die area similar to that of a single LC-tank oscillator, while significantly improving the TR and keeping a reasonable PN performance. The single-tank oscillator employs a strongly coupled transformer-based tank and forces the tank to oscillate either in a differential mode (DM) or common mode (CM); see Figure 7.1(c) [33, 34]. The DM oscillation provides the TR equivalent of a single-tank oscillator. The TR is then *extended* by the CM oscillation. The oscillator has two separate active circuits to excite each mode. However, since the passive part is shared in both modes, the die area is comparable to that of a typical narrow TR oscillator.

In Section 7.2, we briefly analyze the mode-switching oscillator introduced in [20]. Section 7.3 describes how the transformer-based tank can exhibit both DM and CM resonances. Section 7.4 describes a circuit implementation of the single-tank two-core oscillator that excites one of these resonances at a time. Section 7.5 shows measurement results.

## 7.2 Mode-Switching Oscillator

As we mentioned before, in this technique, two capacitively and magnetically coupled LC resonators are replaced a simple resonator to widen oscillator bandwidth. The input impedance of the transformer-based tank, shown in Figure 7.2(a), has a fourth-order polynomial denominator and shows two resonant frequencies,

$$\omega_{L,H}^2 = \frac{1 + X \pm \sqrt{(1+X)^2 - 4X\left(1 - k_m^2\right)}}{2\left(1 - k_m^2\right)}\omega_2^2, \tag{7.1}$$

where $\omega_1^2 = \frac{1}{L_1 C_1}$, $\omega_2^2 = \frac{1}{L_2 C_2}$ and $X = \frac{L_2 C_2}{L_1 C_1}$. The oscillator built around a transformer tank can excite $\omega_L$ or $\omega_H$ at a time to expand its tuning range. However, the different impedances of these resonances (see Figure 7.2(b)) results in a large gap in PN performance of the oscillator in two modes.

A tank can also be capacitively coupled as shown in Figure 7.2(c). Two sides of the transformer can be forced to oscillate either in phase or 180° out of phase with the help of four switches (see Figure 7.3(a)) [20]. When

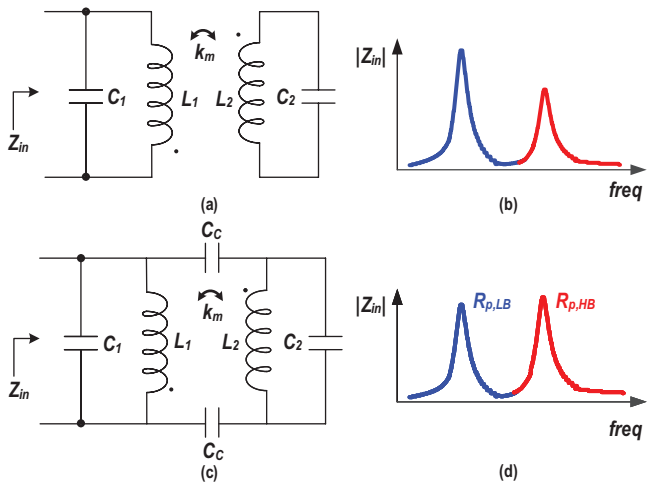


**Figure 7.2** (a) Transformer-based tank and (b) its input impedance; (c) capacitively coupled transformer-based tank and (d) its input impedance.

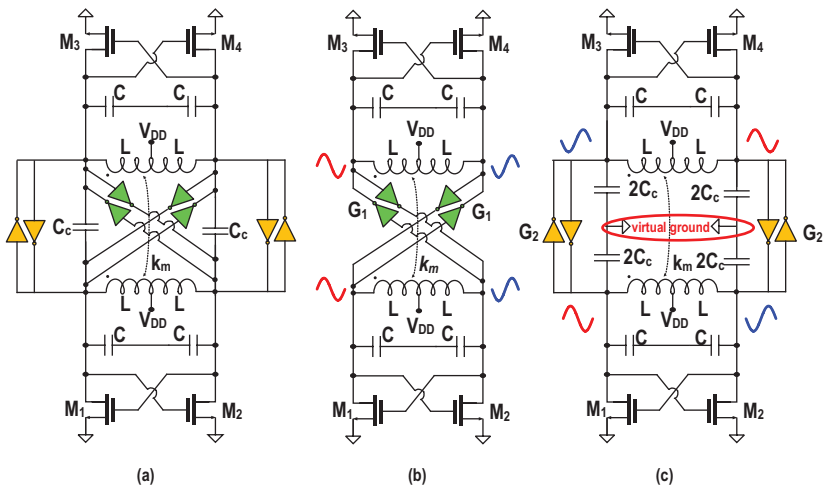


**Figure 7.3** (a) Simplified schematic of DCO; (b) DCO operates in HB; and (c) LB.

oscillation is in phase, high-frequency band (HB), the coupling capacitor cannot be seen. Assuming $L_1 = L_2 = L$ and $C_1 = C_2 = C$,

$$\omega_{HB} = \frac{1}{\sqrt{(1-k_m)LC}}. \tag{7.2}$$

However, if the two sides of the transformer are forced to oscillate out of phase, there will be a virtual ac ground in the middle of $C_C$, as shown in Figure 7.3(c). Therefore, the oscillator is switched to the low-frequency band (LB). The output frequency is obtained as follows:

$$\omega_{LB} = \frac{1}{\sqrt{(1+k_m)L(C+C_C)}}, \tag{7.3}$$

where $C_C$ is the coupling capacitance between the two windings. A low coupling factor of the transformer, $k_m$, ensures that the separation between high-band and low-band frequencies is in a way that a continuous oscillation is possible. The equivalent parallel resistance of the two modes of the resonators can be found as follows [20]:

$$R_{p,HB} \approx \frac{(1-k_m)\,L}{C \cdot r_s} \tag{7.4}$$

$$R_{p,LB} \approx \frac{(1+k_m)\,L}{(C+C_c) \cdot r_s}, \tag{7.5}$$

in which $r_s$ is the equivalent series resistance of the primary and secondary inductances. These four design parameters, $k_m$, $C_C$, $C$, and $L$, are used to design an oscillator with continuous tuning range and some frequency overlap between the oscillation modes, while making possible $R_{p,HB} \approx R_{p,LB}$ (Figure 7.2(d)) to ensure balanced performance in the two modes.

The coupled tank resonates at one of these modes (bands) depending on the $G_1$ and $G_2$ transconductances states (see Figure 7.3(a)). When $G_1$'s are on and $G_2$'s are off, two sides of the tank oscillate at the same phase. In the opposite state, $G_1$'s are off and $G_2$'s are on, so the two sides of the resonator oscillate out of phase. In order to avoid the frequency discrepancy between HB and LB, $C_C$ and $k_m$ are chosen to provide some frequency overlap between the two oscillation bands and also assure almost equable phase noise performance in both modes [20]. The transconductances are designed as differential cells as is shown in Figure 7.4.

We designed a wide tuning range oscillator with this technique. It employs a transformer with $L = 700$ pH and $k_m = 0.18$ [32]. The transformer characteristics are shown in Figure 7.5(a–c). $L_1$ and $L_2$ are well designed to have more or less the same inductance. Although $L_2$ is considerably larger than $L_1$, however its quality, $Q_2$, factor is still 1.7 times less than $Q_1$.

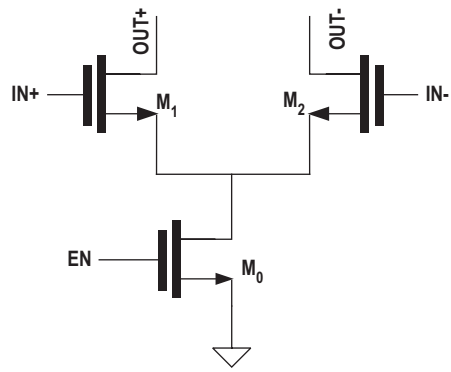


**Figure 7.4** Differential transconductance schematic.

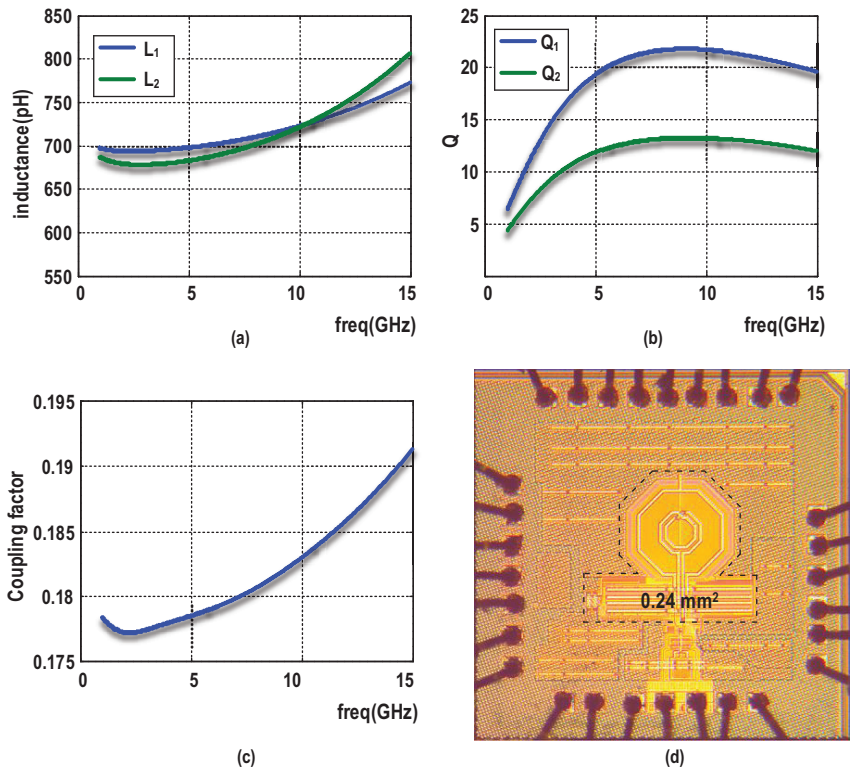


**Figure 7.5** (a) Inductance and (b) quality factor of the transformer's primary and secondary winding. (c) The coupling factor. (d) Chip micrograph.

The oscillator is designed and realized in SMIC 40 nm 1P7M CMOS process. $V_{DD}$ is chosen to be 0.6 V and the oscillation frequency is 3.6–5.02 GHZ (32% tuning range) in LB and 4.6–6.94 GHz (40% tuning range) in HB, resulting in a total of 65% tuning range. The PN performance of the $f_{max}$, $f_{mid}$, and $f_{min}$ in LB and HB modes are shown in Figure 7.6 and Figure 7.7, respectively.

The $M_1$–$M_4$ transistor sources are connected to ground; consequently, the amount of tank's current harmonic is relatively large. In agreement with our discussion in Chapter 5, the 1/f$^3$ corner is relatively large in this oscillator. For the same reason, the frequency pushing of this oscillator is also relatively high as is measured and shown in Figure 7.8.

The chip micrograph is shown in Figure 7.5(d). Active die area is about 0.24 mm$^2$ which is about two times larger than the rest of single tank oscillators we studied so far in this book. In Section 7.3, we study in detail a dual mode wide tuning range oscillator with an area of a single tank oscillator.

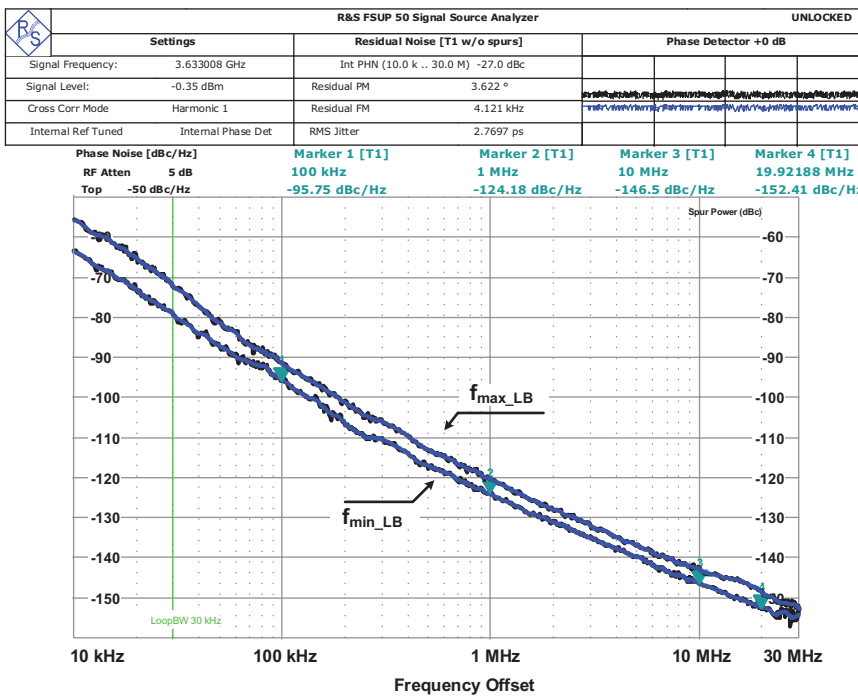


**Figure 7.6** PN of the oscillator in the LB.

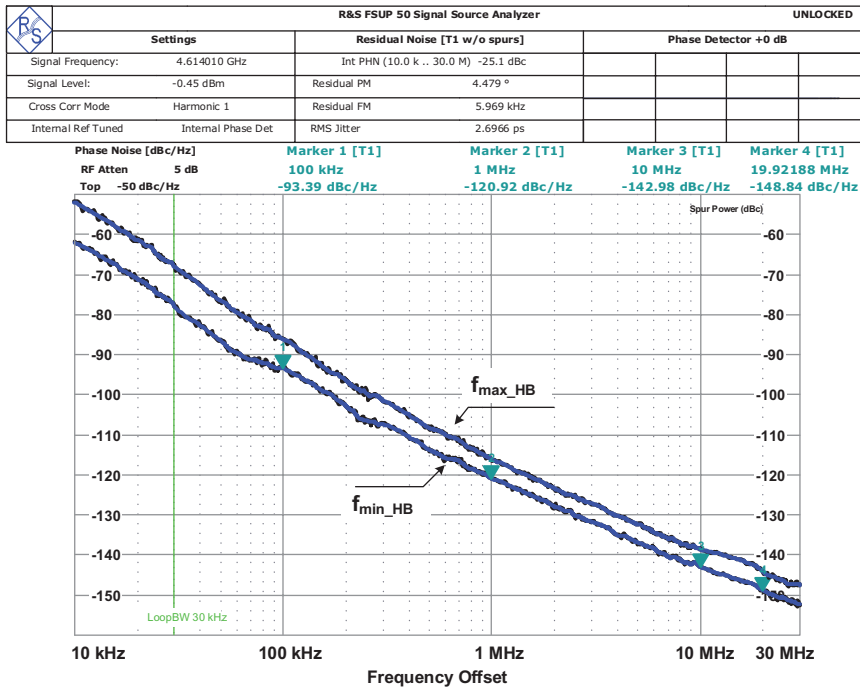


**Figure 7.7** PN of the oscillator in the HB.

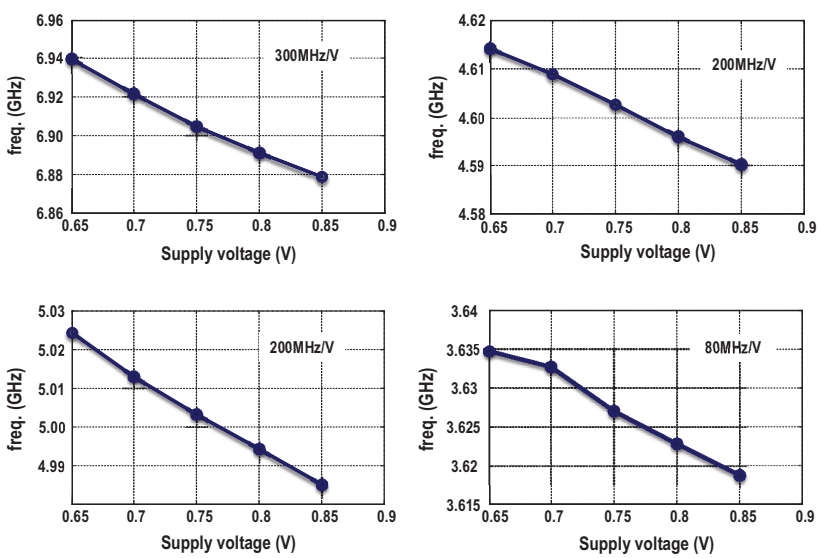


**Figure 7.8** Oscillation frequency dependency on supply voltage for different frequency bands.

## 7.3 Common-Mode Resonances

A transformer-based tank, depicted in Figure 7.9(a), exhibits two DM resonant frequencies. If this transformer possesses a strong magnetic coupling factor, $k_m$, its leakage inductance would be small and so the second DM resonant frequency would be much higher than the main one. Consequently, we would not get a continuous extension of the TR by forcing the oscillation at the second DM resonant frequency. On the other hand, in order for the transformer size to be not much larger than that of an inductor,

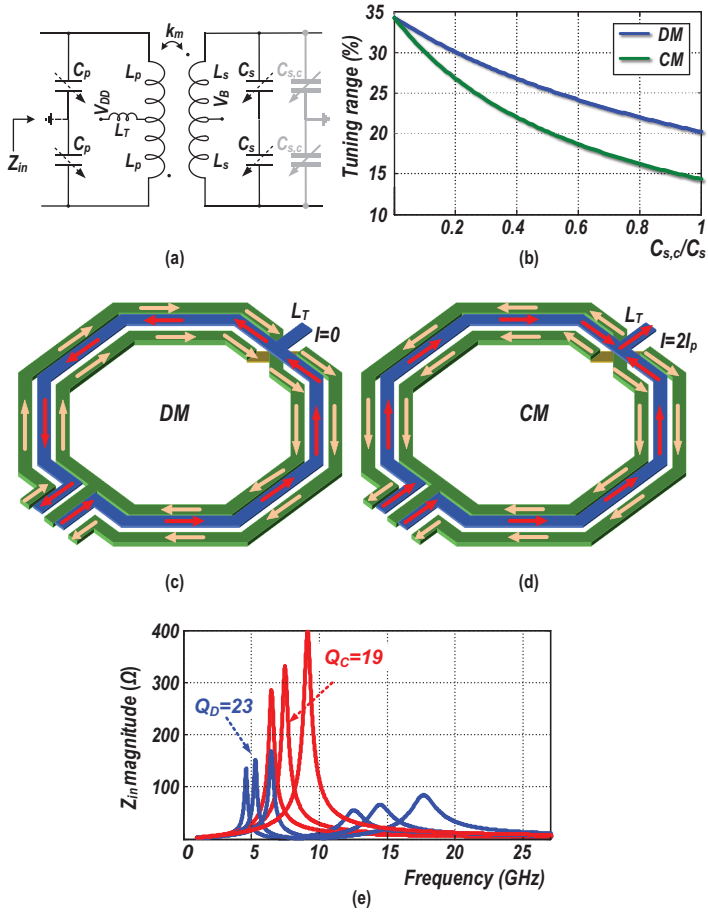


**Figure 7.9** (a) A transformer-based tank; (b) limited DM and CM TR due to $C_s, c$; 1:2 turn transformer: (c) DM excitation; (d) CM excitation; and (e) tank's input impedance.

$k_m > 0.6$ appears a necessary condition. With this constraint, the first resonance can be estimated as [24]

$$\omega_{0,DM} \approx \frac{1}{\sqrt{L_p C_p + L_s C_s}}, \tag{7.6}$$

where $L_p$ and $C_p$ are primary, and $L_s$ and $C_s$ are secondary windings' inductances and capacitances. The approximation error of (7.6) from the exact resonant frequency (Equation (5) in [24]) is less than $+6\%$ for $k_m \geq 0.7$.

Abandoning the hope of exploiting the second DM resonance, suppose now this tank is excited by CM signals, and, for now, we assume that primary and secondary winding inductances and $k_m$ are similar in DM and CM excitations. CM signals cannot see the differential capacitors; thus, the tank can only exhibit CM resonances when these capacitors are single-ended. If this tank were to employ only single-ended primary and *differential* secondary capacitors, the secondary winding inductances and capacitances would not affect the CM characteristics of the tank, e.g., resonant frequency. This tank will show a single CM resonance at

$$\omega_{0,CM} \approx \frac{1}{\sqrt{L_p C_p}}. \tag{7.7}$$

The difference between the CM and DM resonance frequencies, i.e., Equations (7.7) and (7.6), suggests a new possibility for extending the tuning range toward higher frequencies, provided we can build an oscillator around this transformer-based tank that can excite it with either DM or CM signals, without adding any bulky passive components. To investigate how much tuning range we can expect from a single tank, we assume that the tank employs a switched capacitor bank with a 2:1 capacitance switching ratio:

$$C_{p,max}/C_{p,min} = C_{s,max}/C_{s,min} = 2. \tag{7.8}$$

This ratio should guarantee a sufficiently high Q-factor of switched-capacitors in recent CMOS technologies. With this assumption, $f_{max}/f_{min} = \sqrt{2}$ in both modes and, thus, both DM and CM resonant frequencies (Equations (7.6) and (7.7)) will tune by $2(\sqrt{2}-1)/(\sqrt{2}+1) = 34.3\%$. To avoid any gaps between the DM and CM tuning ranges, at least $\omega_{CM,low} = \omega_{DM,high}$. Hence,

$$L_p C_{p,max} = L_s C_{s,max}. \tag{7.9}$$

With these conditions, the resonant frequency could theoretically cover an octave while going from DM to CM oscillations. Practically, $C_{max}/C_{min}$ has

to be >2 due to parasitics and difficulty with controlling the precise overlap between the DM and CM resonances.

One limiting factor in the tuning range of such an oscillator is the single-ended parasitic capacitance throughout the secondary winding side. If the CM coupling factor, $k_{m,c}$, were hypothetically similar to the DM one, $k_{m,d}$, and $k_{m,c} = k_{m,d} > 0.6$, then the CM resonance would shift down to $\omega_{0,CM} = 1/\sqrt{L_p C_p + L_s C_{s,c}}$, where $C_{s,c}$ is the total of single-ended capacitances on the secondary side (Figure 7.9(a)). At the same time, the DM resonance would also shift down to $\omega_{DM} = 1/\sqrt{L_p C_p + L_s C_s + L_s C_{s,c}}$. Interestingly, satisfying the overlap between CM and DM oscillations with the condition in (7.8) results in the same constraint as (7.9). However, the fixed parasitic capacitance, $C_{s,c}$, degrades the CM oscillation tuning range more than it degrades the DM oscillation tuning range; see Figure 7.9(b).

A 1:2 turns-ratio transformer, which has distinctly different characteristics in DM and CM excitations, relieves such a degradation. Figures 7.9(c,d) show this transformer when its primary is excited, respectively, with DM or CM signals. In the DM excitation, the induced currents at the two sides of the secondary winding circulate constructively in the same direction, thus creating a strong coupling factor between the transformer windings, while in the CM excitation these induced currents cancel each other within each full turn of the secondary winding (i.e., from the secondary's terminal to the secondary's center-tap), leading to a weak coupling factor [23]. This weak $k_{m,c}$ can be interpreted as the secondary winding not being seen from the primary and, therefore, the secondary's single-ended capacitors have an insignificant effect on the tank's CM resonant frequency.

Assuming the capacitor bank is almost ideal, at least compared to the lossy inductors represented by the $r_p$ and $r_s$ equivalent series resistances of the primary/secondary windings, CM resonance has the quality factor of $Q_{CM} = Q_p = L_p\omega/r_p$, which is similar to that of an inductor-based tank. The high Q-factor of this resonance indicates that with an appropriate active circuitry, the CM oscillation of a reasonable quality would be possible. The DM and CM input impedances of this tank are shown in Figure 7.9(e). The single-ended switched capacitors require two switches to provide a ground connection in the middle, which results in a 50% lower Q-factor as compared to a differential switched capacitor with the same switch size. This would appear as a disadvantage of our new technique; however, that is not the case. Let us compare the tuning range of a typical inductor-based tank oscillator employing the differential capacitor bank with our transformer-based tank oscillator employing the single-ended primary and the differential

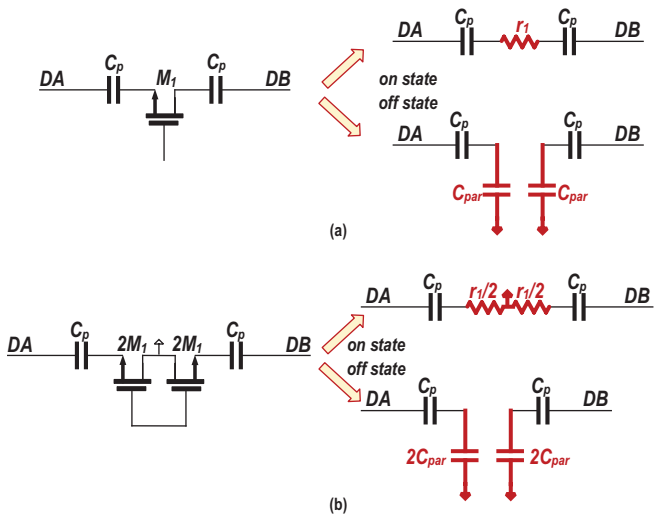


**Figure 7.10** (a) Differential and (b) single-ended capacitor banks.

secondary capacitor banks. The equivalent capacitance of this bank varies from $C_{\text{on,D}} = C_p$ to $C_{\text{off,D}} = \frac{C_p C_{par}}{C_p + C_{par}}$, where $C_{par}$ is the parasitic capacitance of the switch (see Figure 7.10(a)). For a typical $C_{\text{off,D}}/C_{\text{on,D}}$ value of 0.5 ($C_{par} = C_p$), the inductor-based oscillator employing this tank would exhibit $f_{max}/f_{min} = \sqrt{2}$.

The width of each switch in the single-ended switched-capacitor bank should be twice the width of each differential counterpart for the same Q-factor. Consequently, $C_{\text{off,C}} = \frac{2C_p C_{par}}{C_p + 2C_{par}} = \frac{2}{3}C_p$ (see Figure 7.10(b)). Employing this capacitor bank in a transformer-based tank at the primary winding and employing the differential bank at the secondary winding, and benefiting from the impedance transformation of the 1:2 turns-ratio transformer ($L_s/L_p \approx 3$), results in $\frac{f_{max}}{f_{min}} = \sqrt{1.9}$, which is very close to the inductor-based tank tuning range.

## 7.4 Novel Wide Tuning Range Oscillator

### 7.4.1 Dual-Core Oscillator

Forcing the transformer-based tank to resonate in DM is quite straightforward. The oscillator can be realized as a one-port or a two-port structure [25, 26]. However, only the two-port structure will guarantee a reliable

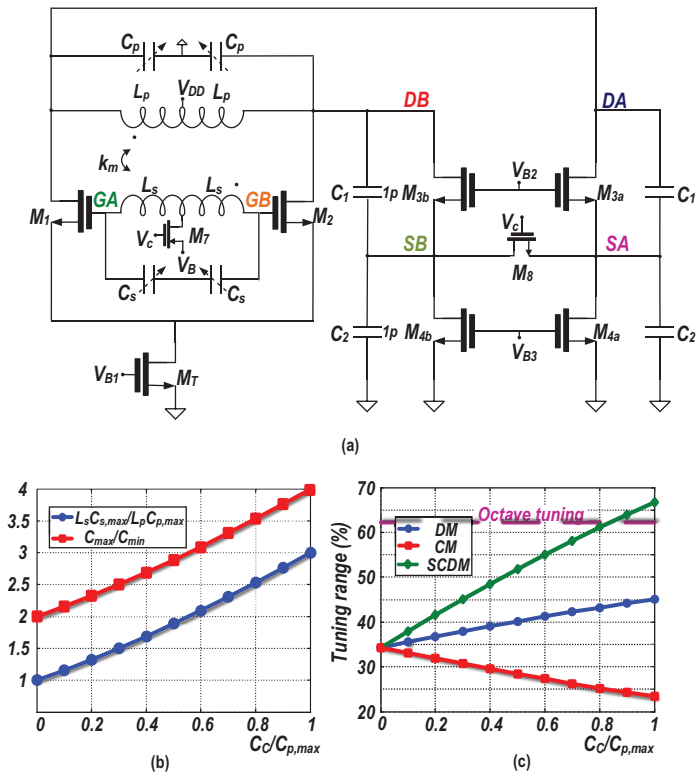


**Figure 7.11** Dual core oscillator: (a) schematic; (b) overlap and octave oscillation conditions; and (c) tuning range.

start-up at the first DM resonance [24], thus preventing the mixed DM oscillation. A separate active circuit is now needed to force the tank into the CM resonance. Colpitts and Hartely topologies are two well-known examples of single-ended oscillators. Invoking our ground principle of sharing the *same* tank by the active CM and DM circuits, the Coplitts structure is consequently chosen. To improve the PN, two mutually injection-locked Colpitts oscillators share the primary inductor. The schematic of the novel dual core oscillator is shown in Figure 7.11(a). To avoid the dual oscillation, only one active circuit core is turned on at a time.

The left side of Figure 7.11(a) is the two-port DM oscillator. In this mode, $V_{B2} = V_{B3} = 0V$, $M_7$ switch is on biasing $M_{1,2}$, while $M_8$ switch is off. The waveforms are shown in Figure 7.12(a,b). The transformer has the 1:2 turns ratio and its gain reduces the $M_{1,2}$ noise upconversion to PN, and also

results in a larger gate voltage compared to drain voltages, which facilitates oscillation start up.

The right-hand side of the oscillator schematic are two locked single-ended Colpitts oscillators. $M_8$ switch is now turned on to ensure the in-phase operation of the two Colpitts oscillators, without which the two cores might exhibit an arbitrary phase shift. In this mode, $V_{B1} = 0V$ to turn off the differential oscillation. $M_7$ switch is also off to minimize the CM inductive loading on the primary winding by the secondary one. Both single-ended oscillators start at the same frequency but could be slightly out of phase; subsequently, they lock to each other and there is no phase shift between them. The locking of the two oscillators gives an additional 3-dB PN improvement. Waveforms are shown in Figure 7.12(c,d).

Note that an attempt of simplifying the CM structure by removing $M_8$ and permanently shorting the sources of $M_3$ transistors would be detrimental to the DM tuning range. While obviously the DM oscillation would still work – $M_3$ transistors are off in this mode – the extra capacitance $C_{fix}$ due to the CM circuitry seen by $C_p$ would be larger. With $M_8$ off, DA/DB node sees

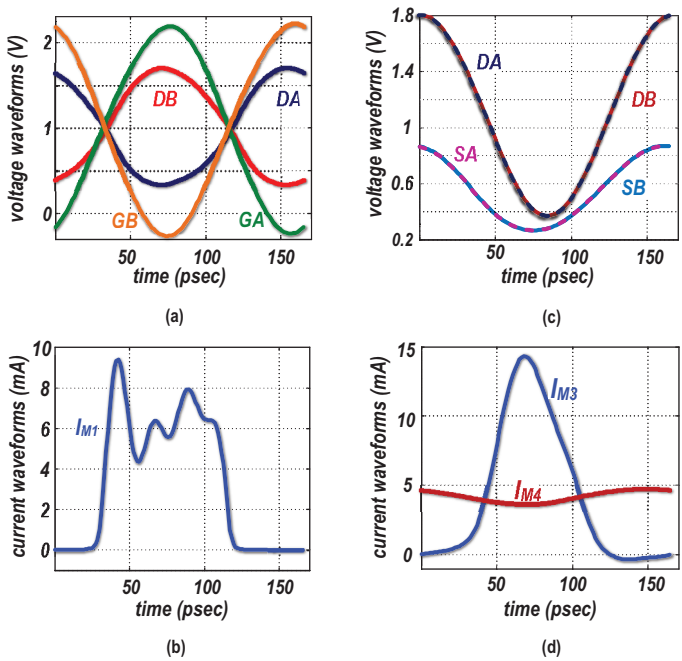


**Figure 7.12** Dual core oscillator waveforms: (a,b) DM and (c,d) CM.

$C_{fix} = C_1C_2/(C_1 + C_2)$, but when $M_3$ sources are shorted, that capacitance raises to $C_{fix} = C_1 > C_1C_2/(C_1 + C_2)$. Furthermore, an attempt of moving $M_8$ from the SA/SB source nodes of $M_3$ to the DA/DB drain nodes would likewise increase the effective parasitic capacitance of $M_8$.

The $C_1$ and $C_2$ capacitors are necessary to create a negative resistance for the Colpitts oscillators; however, they are limiting the tuning range in both modes. In their presence, (7.8) and (7.9) are not valid anymore for the overlap and octave tuning. Assuming the same capacitance variation range on the primary and secondary sides, $C_{p,max}/C_{p,min} = C_{s,max}/C_{s,min}$, the octave tuning requirement is now

$$\frac{L_sC_{s,max}}{L_pC_{p,max}} = 3\frac{C_C}{C_{p,max}} + 4\frac{C_{p,min}}{C_{p,max}} - 1, \tag{7.10}$$

where $C_C = C_1C_2/(C_1+C_2)$. The minimum overlap condition, $f_{DM,max} = f_{CM,min}$, dictates

$$\frac{C_{p,max}}{C_{p,min}} = 1 + \frac{L_sC_{s,max}}{L_pC_{p,max}}. \tag{7.11}$$

Figure 7.11(b) shows how the required $C_{max}/C_{min}$ increases with $C_C/C_p$ ratio. Satisfying (7.11) and (7.10) in the presence of $C_C$ also unbalances the DM and CM tuning range, as shown in Figure 7.11(c). For a certain value of $C_C$, the required $C_{p,max}/C_{p,min}$ ratio can become prohibitively large, likely leading to the Q-factor degradation. In practice, $C_{s,max}/C_{s,min}$ and $C_{p,max}/C_{p,min}$ should not be necessarily equal. The secondary-winding capacitor ratio in this design is chosen to be larger than at the primary side due to the tougher Coplitts oscillator start-up conditions.

### 7.4.2 Phase Noise Analysis

Ideally, a wide TR oscillator would have a comparable PN performance in both oscillation modes. In this section, we investigate the PN of the dual core oscillator and then compare the two modes.

The linear time-variant model [28] suggests

$$\mathcal{L}(\Delta\omega) = 10\log_{10}\left(\frac{kT}{R_tNq_{max}^2(\Delta\omega)^2}\cdot F\right), \tag{7.12}$$

where $k$ is Boltzmann's constant, $T$ is temperature, $R_t$ is the equivalent parallel resistance of the tank, and $q_{max}$ is the maximum charge displacement across the equivalent capacitance in parallel to $R_t$. $N$ is the number of

resonators, which is 2 here in both DM and CM oscillators. $F$, the oscillator's effective noise factor, is

$$F = \sum_i \frac{N \cdot R_t}{2kT} \cdot \frac{1}{2\pi} \int_0^{2\pi} \Gamma_i^2(\phi)\, \overline{i_{n,i}^2(\phi)}\, d\phi, \tag{7.13}$$

in which $\Gamma_i$ is the ISF of the $i$th noise source. The relevant ISF of noise sources associated with a sinusoidal waveform oscillator can be estimated by a $\pi/2$ phase shifted sinusoidal function, $\Gamma = \frac{sin(\phi)}{N}$, where $\phi = \omega_0 t$ [27]. Here, we try to find the noise factors of different noise sources in the dual core oscillator.

The noise sources of the Colpitts oscillator are $R_t$, $M_3$, and $M_4$. $R_t$ in the CM oscillation is the parallel resistance of the primary winding, $R_p$. It is insightful to refer every noise source and nonlinearity back to the tank, as it is demonstrated step-by-step in Figure 7.13. The negative conductance between $DA$ and $SA$ nodes is

$$g_n = \frac{i_{d3}}{v_{DA} - v_{SA}} = \frac{-g_{m3} v_{SA}}{v_{DA} - v_{SA}} = -g_{m3} \frac{C_1}{C_2}, \tag{7.14}$$

where $i_{d3}$ is the small-signal drain current of $M_3$. The equivalent negative conductance in parallel with the tank is found as

$$G_n = \left(\frac{C_2}{C_1 + C_2}\right)^2 \cdot g_n = -g_{m3} \frac{C_1 C_2}{(C_1 + C_2)^2}. \tag{7.15}$$

With a similar derivation, $M_3$ channel resistance is referred to the tank as

$$R_{ds3} = r_{ds3} \left(\frac{C_1 + C_2}{C_2}\right)^2. \tag{7.16}$$

To sustain the oscillation, the average dissipated power in the tank loss and $R_{ds3}$ should be equal to the average power delivered by the negative resistance, which leads to the condition:

$$G_{mEF3} = \frac{1}{n(1-n)} \cdot \frac{1}{R_p} + \frac{1-n}{n} \cdot G_{dsEF3}, \tag{7.17}$$

where $n = C_1/(C_1 + C_2)$, $G_{mEF} = G_m[0] - G_m[2]$, and $G_{dsEF} = G_{ds}[0] - G_{ds}[2]$, in which $G_m[k]$ and $G_{ds}[k]$ are the $k$th Fourier coefficients of $g_m(t)$ and $g_{ds}(t)$, respectively [29]. The required $G_{mEF3}$ is minimized for $n = 0.5$, which is chosen in this design to facilitate start-up.

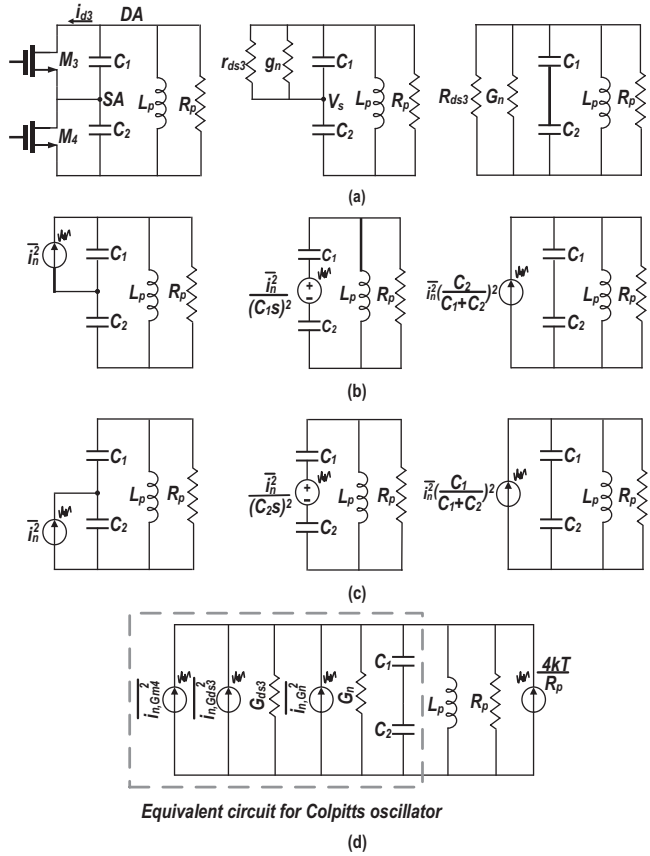


**Figure 7.13** Procedures of referring the noise back to the tank from: (a) $r_{ds3}$ and negative conductance; (b) $g_m$ of $M_3$; and (c) $g_m$ of $M_4$. (d) The equivalent circuit of the Colpitts oscillator.

To refer the current noise sources to the tank, they are first converted to their Thevenin voltage source equivalents and then converted back to Norton current source equivalents, as demonstrated in Figure 7.13(b) and (c). The equivalent noise of $M_3$ and $M_4$'s transconductance then becomes

$$\overline{i_{n3}^2} = 4kT\gamma g_{m3}\left(\frac{C_2}{C_1+C_2}\right)^2, \tag{7.18}$$

$$\overline{i_{n4}^2} = 4kT\gamma g_{m4}\left(\frac{C_1}{C_1+C_2}\right)^2, \tag{7.19}$$

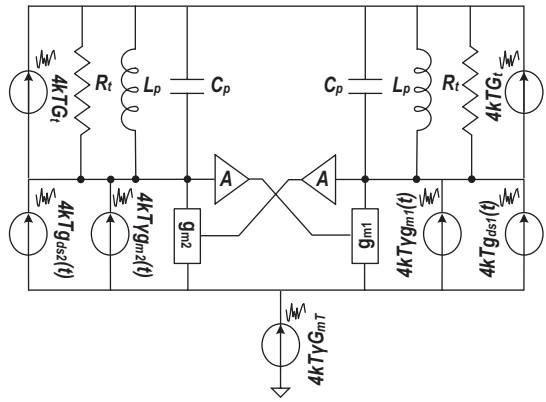


**Figure 7.14** Noise sources of the DM oscillator [24].

where $\gamma$ is the transistor excess noise coefficient. Assuming a sinusoidal oscillation, the tank noise factor is found as

$$F_t = \frac{2N}{2kTR_p} \cdot \frac{1}{2\pi} \int_0^{2\pi} \frac{4kT}{R_p} \frac{\sin^2(\phi)}{N^2} \, d\phi = 1. \tag{7.20}$$

$M_3$ and $M_4$ noise factors are found as

$$\begin{aligned} F_{gm3} &= \frac{2NR_p}{4kT\pi} \int_0^{2\pi} \frac{\sin^2(\phi)}{N^2} 4kT\gamma g_{m3}(\phi) \cdot \left( \frac{C_2}{C_1 + C_2} \right)^2 d\phi \\ &= (1-n)^2 \gamma G_{mEF3} R_P \end{aligned} \tag{7.21}$$

$$\begin{aligned} F_{gds3} &= \frac{2NR_p}{4kT\pi} \int_0^{2\pi} \frac{\sin^2(\phi)}{N^2} 4kT\gamma g_{ds3}(\phi) \cdot \left( \frac{C_2}{C_1 + C_2} \right)^2 d\phi \\ &= (1-n)^2 G_{dsEF3} R_p \end{aligned} \tag{7.22}$$

$$\begin{aligned} F_{gm4} &= \frac{2NR_p}{4kT\pi} \int_0^{2\pi} \frac{\sin^2(\phi)}{N^2} 4kT\gamma g_{m4} \cdot \left( \frac{C_1}{C_1 + C_2} \right)^2 d\phi \\ &= n^2 \gamma G_{mEF4} R_P \end{aligned} \tag{7.23}$$

$g_{ds4}$ noise is very small due to $M_4$ operating in a saturation region and, consequently, is disregarded in our calculations. Since $g_{m4}$ is fairly constant throughout the period, $G_{mEF4} = g_{m4}$. To estimate the contribution of $M_4$ to PN, we can calculate $g_{m4}$ as

$$g_{m4} = \frac{2I_0}{V_{gs4} - V_{th}} \approx \frac{2I_0}{V_{ds,min}}, \tag{7.24}$$

where $V_{th}$ is the transistor's threshold voltage. Let us assign $V_{DD}/2$ to the SA (SB) node, and $V_{DA} \approx 2I_0R_p(1-n)$ [27],

$$g_{m4} \approx \frac{4I_0}{V_{DD} - 4n(1-n)I_0R_p}. \tag{7.25}$$

Disregarding $g_{ds4}$ noise contribution,

$$F_{M4} \approx F_{gm4} = \frac{4n^2\gamma R_pI_0}{V_{DD} - 4n(1-n)I_0R_p} \approx \gamma. \tag{7.26}$$

By substituting (7.17) in (7.21), with $G_{mEF3}$ and $G_{dsEF3}$ numerically obtained from simulations, the total oscillator effective noise factor then will be

$$F_{CM} = R_P\left[(1-n)^2G_{mEF3}\left(\gamma + \frac{n}{1-n}\right) + \frac{4n^2\gamma I_0}{V_{DD} - 4n(1-n)I_0R_p}\right] - 1 \approx 2.2\gamma + 0.2. \tag{7.27}$$

The circuit-to-phase-noise conversion of the CM oscillator is shown in Figure 7.15(a–d).

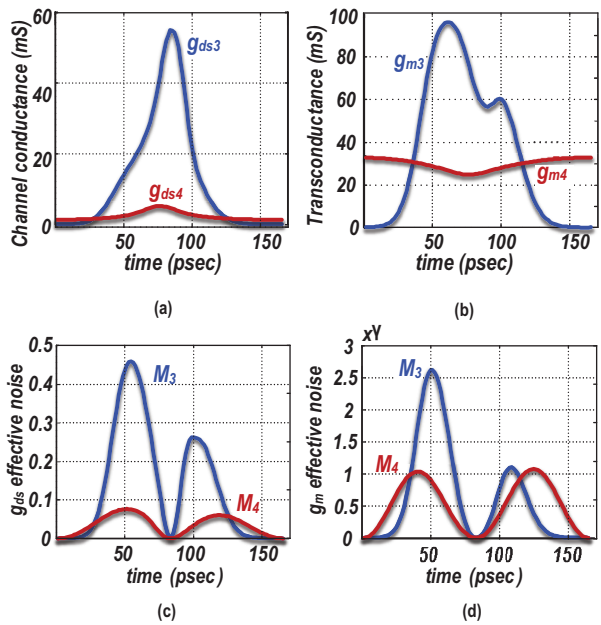


**Figure 7.15** Circuit-to-phase-noise conversion in CM oscillator.

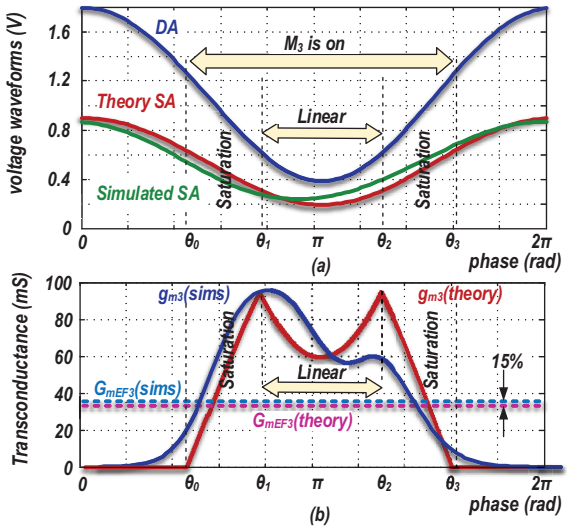


**Figure 7.16** (a) Drain and source voltage waveforms. (b) $g_{m3}$: theory and simulations.

The noise contribution of $M_3$ transistor can be numerically calculated based on design parameters. For $M_3$, $V_d(\phi) = V_{DD} + A_C\cos(\phi)$, $V_s(\phi) \approx V_{DD}/2 + nA_C\cos(\phi)$ and $V_g = V_{B2}$. Figure 7.16 shows the $M_3$ operating regions during one oscillating period. At $\theta_0$, $V_s$ gets low enough for $M_3$ to turn on and enter the saturation region. When the drain voltage gets lower, $M_3$ enters the triode region at $\theta_1$ and remains there till $\theta_2 = 2\pi - \theta_1$. $M_3$ finally turns off again at $\theta_3 = 2\pi - \theta_0$. $\theta_0$ and $\theta_1$ can be found from boundary conditions as

$$\theta_0 = \cos^{-1}\left(\frac{V_1}{nA_C}\right) \tag{7.28}$$

and

$$\theta_1 = \cos^{-1}\left(\frac{V_2}{A_C}\right) \tag{7.29}$$

where $V_1 = V_{B2} - V_{DD}/2 - V_{th}$ and $V_2 = V_{B2} - V_{DD} - V_{th}$.

Assuming square law,

$$g_{m3}(\phi) = \begin{cases} K(V_1 - nA_C\cos(\phi)) & \text{saturation,} \\ K(\frac{V_{DD}}{2} + (1-n)A_C\cos(\phi)) & \text{linear,} \\ 0 & \text{cut-off,} \end{cases} \tag{7.30}$$

where $K = \mu C_{ox}\left(\frac{W}{L}\right)$ is the customary designation of MOS transistor strength. $G_{mEF3}$ now can be determined by calculating the Fourier coefficients of $g_{m3}(\phi)$. Solving the lengthy integrations results in

$$\begin{aligned} G_{mEF3} = \frac{K}{2\pi}[&2V_1(\theta_1-\theta_0)+V_{DD}(\pi-\theta_1)+nA_c\sin(\theta_0)-A_c\sin(\theta_1) \\ &+V_1\sin(2\theta_0)+\left(\frac{V_{DD}}{2}-V_1\right)\sin(2\theta_1)-\frac{nA_c}{3}\sin(3\theta_0) \\ &+\frac{A_c}{3}\sin(3\theta_1). \end{aligned} \tag{7.31}$$

$G_{mEF3}$ in (7.31) can be calculated by substituting $\theta_0$ and $\theta_1$ from (7.28) and (7.29), together with other design parameters: $V_{DD} = 1.1$ V, $V_{B2} = 1$ V, $V_{th} \approx 0.37$ V. Figure 7.16(b) shows a very good agreement (within 15%) with the simulation results.

Major noise sources of the DM oscillator are shown in Figure 7.14. A general result of the effective noise factor, assuming that the $M_T$ thermal noise is completely filtered out, is derived in [24] as

$$2\Gamma_{t,rms}^2 \cdot \left(1+\frac{\gamma}{A}\right)\cdot(1+R_tG_{dsEF1}) \approx 1.6+0.9\gamma. \tag{7.32}$$

However, the $M_T$ thermal noise is not completely filtered out here. To calculate the $M_T$'s noise contribution, the tail node ISF is obtained through simulations and plotted in Figure 7.17(e). From that

$$F_{M_T} = \frac{1}{2\pi}\int_0^{2\pi} 4kT\gamma g_{mT}\cdot\Gamma_{M_T}^2(t)\,\frac{R_t}{4kT}\,dt \approx 0.5\gamma. \tag{7.33}$$

Hence, the DM oscillator noise factor is

$$\begin{aligned} F_{DM} = &2\Gamma_{t,rms}^2\cdot\left(1+\frac{\gamma}{A}\right)\cdot(1+R_tG_{dsEF1}) \\ &+\Gamma_{M_T,rms}R_pG_{MTEF} \approx 1.6+1.4\gamma. \end{aligned} \tag{7.34}$$

The DM oscillator circuit-to-phase-noise conversion is shown in Figure 7.17(a–d).

Substituting (7.27) and (7.34) in (7.12) at the *overlap* frequency results in

$$\mathcal{L}_{DM}-\mathcal{L}_{CM} = 10\log_{10}\left(\frac{R_tQ_pA_C^2}{R_pQ_tA_D^2}\cdot\frac{F_{DM}}{F_{CM}}\right) \approx -2.5\ \text{dB}. \tag{7.35}$$

Due to its single-ended structure and the CM resonance, the Colpitts oscillator would appear to be more sensitive to supply noise. However, that is

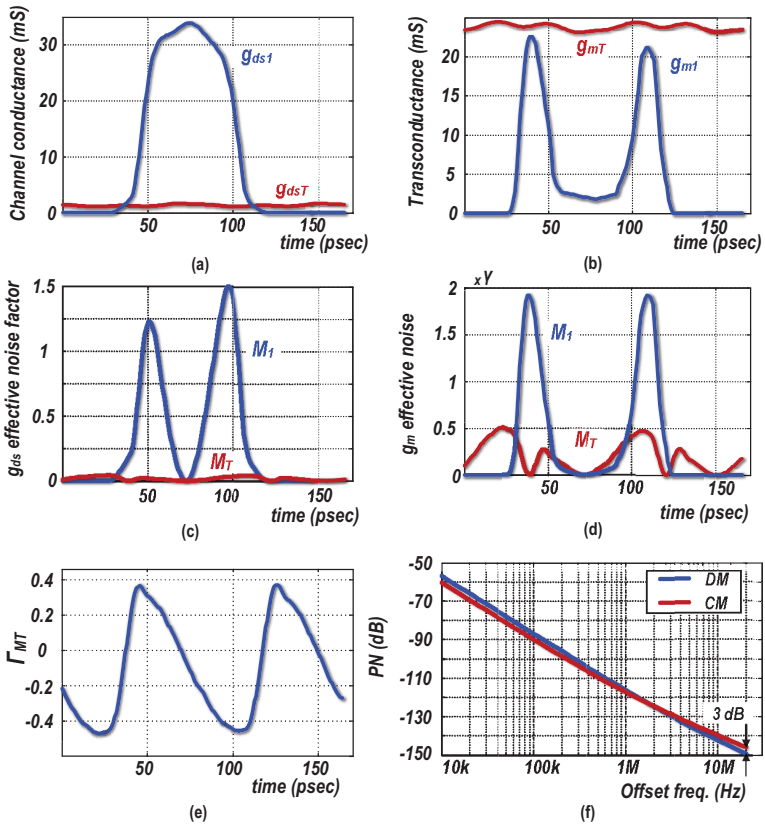


**Figure 7.17** (a–d) Circuit-to-phase-noise conversion in DM oscillator; (e) tail transistor ISF; and (f) PN of CM and DM oscillators at the overlap frequency.

not the case. Supply pushing is the parameter that indicates the supply noise effect on the phase noise. Figure 7.19(e,f) demonstrates this parameter for the DM and CM oscillators, which is quite comparable, indicating that the CM oscillation does not result in higher phase noise upconversion sensitivity to the supply noise. To explain that, let us look at the actual mechanism: the oscillation frequency can be modulated by the supply noise by modulating the nonlinear voltage-dependent parasitic capacitors of the core transistors, $C_{gs}$. In the Colpitts oscillator, the supply voltage is connected to the core transistors' drains, which cannot modulate their $C_{gs}$ directly. Consequently, the oscillation frequency modulation due to the supply noise is considerably reduced.

### 7.4.3 Center Tap Inductance

The single-ended nature of the Colpitts oscillator makes its characteristics especially sensitive to single-ended parasitics. A key parasitic that must be properly modeled and accounted for is the metal track inductance, $L_T$, which connects the center tap of the transformer's primary to the supply's AC-ground (see Figure 7.9(a)). At the DM excitation, the AC current will not flow into $L_T$; thus, the DM inductance and DM resonant frequency are independent of its value. However, at the CM excitation, the current flowing into $L_T$ is twice the current circulating in the inductors. Consequently, the tank inductance $L_p$ in Figure 7.9(a) is re-labeled as $L_{pd} = L_p$ in DM and $L_{pc} = L_{pd} + 2L_T$ in CM excitations. The CM oscillation frequency will be reduced to $\omega_{CM} = 1/\sqrt{(L_p + 2L_T)C_P}$. This implies that $L_T$ must be carefully modeled and included in simulations, otherwise the increased overlap between CM and DM oscillations would severely limit the total tuning range.

Another important parasitic that is only influential in the CM oscillation is the supply loop resistance between the $V_{DD}$ feed to the center-tap of the primary winding and the sources of $M_4$ transistors (see Figure 7.11), assuming sufficient decoupling capacitance on $V_{DD}$. This resistance is added directly to the equivalent negative resistance of the Colpitts structure and increases it from $-g_{m3}/C_1C_2\omega^2$ to $-g_{m3}/C_1C_2\omega^2 + r_b$. In our design, the average of that negative resistance at 6 GHz with $C_1 = C_2 =$1 pF is about $-25\ \Omega$, which means the $r_b$ parasitic resistance should be kept much smaller as to not endanger the start-up.

## 7.5 Experimental Results

The novel oscillator is prototyped in TSMC 40 nm 1P7M CMOS process with top ultra-thick metal. $M_{1,2}$ are (60/0.27) μm and $M_{3,4}$ are (128/0.04) μm low-$V_{th}$ devices for safe start-up of the Colpitts oscillator. The tank employs a 1.4 nH secondary inductor with Q of 25 at 5 GHz and 0.54-nH primary inductor with Q of 17 at 5 GHz. $k_{m,DM} = 0.72$ and $k_{m,CM} = 0.29$. The transformer size is 250 × 250 $\mu m^2$ and the primary-to-secondary winding spacing is 5 μm. The chip micrograph and transformer characteristics are shown in Figure 7.18, respectively. The oscillator's core area is 0.12 $mm^2$, which is similar in size to typical narrow tuning-range oscillators. The tank is shared in the two modes of oscillation and so the output is common; hence, no further multiplexing is necessary. A comparison with other relevant wide

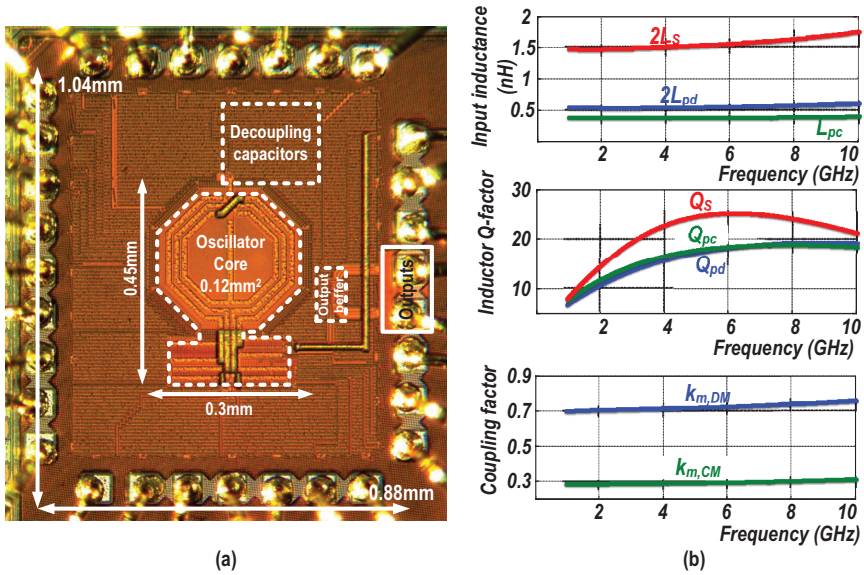


**Figure 7.18** Transformer characteristics.

**Table 7.1** Performance summary and comparison with relevant oscillators

| | | This Work | | [20] | | [21] | | [4] | | [5] | | [13] | | [14] |
|---|---|---|---|---|---|---|---|---|---|---|---|---|---|---|
| Frequency (GHz) | | **3.37–5.96** | | 2.5–5.6 | | 3.24–8.45 | | 2.4–5.3 | | 1.3–6 | | 3.28–8.35 | | 3.14–6.44[2] |
| Tuning range (%) | | **55.5** | | 76 | | 89 | | 75.3 | | 128 | | 87.2 | | 69[2] |
| $V_{DD}$ (V) | | **1** | | 0.6 | | 0.8 | | 0.4 | | 1.5 | | 1.6 | | 1.2 |
| Technology | | **40 nm** | | 65 nm | | 40 nm | | 65 nm | | 130 nm | | 130 nm | | 180 nm |
| OSC core area | | **0.12 mm²** | | 0.29 mm² | | 0.43 mm² | | 0.25 mm² | | 0.295 mm² | | 0.1 mm² | | 0.35 mm² |
| | | $f_{min}$ | $f_{max}$ | $f_{min}$ | $f_{max}$ | $f_{min}$ | $f_{max}$ | $f_{min}$ | $f_{max}$ | $f_{min}$ | $f_{max}$ | $f_{min}$ | $f_{max}$ | $f_{mid}$ |
| $P_{DC}$ (mW) | | **16** | **12.5** | 14.1 | 9.9 | 16.5 | 14 | 6 | 4.4 | 4.35[1] | 9.15[1] | 15.4 | 6.5 | 8.8 |
| PN (dBc/Hz) | 100 kHz | **–103** | **–90** | –101.1 | –89 | –109 | –91 | –98 | –86 | NA | NA | –96 | NA | –92 |
| | 10 MHz | **–149.7** | **–137.8** | –151.9 | –145.8 | –150 | –142 | –149 | –139 | –135 | –132 | –142 | –137.2 | –140 |
| FoM† (dB) | 100 kHz | **181.8** | **174.5** | 177.6 | 174 | 187 | 178.1 | 177.8 | 174.1 | NA | NA | 174.4 | NA | 175.4 |
| | 10 MHz | **188.2** | **182.3** | 188.4 | 190.8 | 188 | 189.1 | 188.8 | 187 | 171 | 178 | 180.4 | 187.5 | 183.4 |
| FoMA†† (dB) | 100 kHz | **191** | **183.7** | 182.9 | 179.4 | 190.7 | 181.7 | 183.8 | 180.1 | NA | NA | 184.4 | NA | 180 |
| | 10 MHz | **197.4** | **191.5** | 193.7 | 196.2 | 191.7 | 192.7 | 194.8 | 193 | 176.2 | 183.2 | 190.4 | 197.5 | 188 |
| FoMAT††† (dB) | 100 kHz | **205.6** | **198.6** | 200.5 | 197 | 209.7 | 200.7 | 201.3 | 197.6 | NA | NA | 203.3 | NA | 196.8 |
| | 10 MHz | **212.3** | **206.4** | 211.3 | 213.8 | 210.7 | 219.7 | 212.3 | 210.5 | 198.3 | 205.4 | 209.3 | 216.3 | 204.8 |

†$FoM = |PN| + 20\ log_{10}(\omega_0/\Delta\omega) - 10\ log_{10}(P_{DC}/1mW)$.

††$FoMA = |PN| + 20\ log_{10}(\omega_0/\Delta\omega) + 10log(1mm/A) - 10\ log_{10}(P_{DC}/1mW)^2$.

†††$FoMAT = |PN| + 20\ log_{10}(\omega_0/\Delta\omega) + 20\ log_{10}(TR/10) + 10log(1mm^2/A) - 10\ log_{10}(P_{DC}/1mW)$.

[1] Including bias circuitry.

[2] Before frequency division.

tuning-range oscillators is summarized in Table 7.1. This oscillator is smaller by at least a factor of 2. The oscillators are tuned via 4-bit switched MOM capacitor banks at the primary and secondary. According to post-layout circuit-level simulations, the tuning range is 46% in DM and 20% in CM, with a 100 MHz overlap, giving the total TR of 63%.

However, measurements show that DM oscillator is tunable between 3.37 and 5.32 GHz (45% TR) and the CM oscillator is tunable between 5.02 and 5.96 GHz (17% TR) and the overlap between the DM and CM oscillations is wider than expected, resulting in a tuning range of 55.5%.

Figure 7.19 shows PN at $f_{max}$ and $f_{min}$ frequencies of the DM and CM oscillations. In both modes, $V_{DD}$ is 1.1 V. Figure 7.19 also reports the PN and FoM of this oscillator over the tuning range. The FoM increases from 188.2 to 189.4 dB in the DM and from 181.3 to 182.3 dB in the CM tuning ranges. The PN in the CM mode is worse than that in the DM mode, but it is worth mentioning that not all applications demand ultra-low phase noise in all bands and channels uniformly.

Table 7.1 also compares FoMA, introduced in [31], of this oscillator with other relevant oscillators. The DM oscillator shows the best FoMA and the CM oscillator's FoMA is comparable with the other state-of-the-art oscillators.

### 7.5.1 Supply and Ground Routing Inductances and Losses

The measurement results deviate from the simulations and theory in two ways. The first is the wider overlap between the DM and CM oscillation frequencies. The second is the degraded PN in the CM Colpitts oscillator. To explain the performance degradation, we first take a closer look at a layout of the transformer-based tank. As revealed in Figure 7.20, the CM inductance should also include the impedance of the current return route, from the center-tap of the primary winding to the sources of $M_{4a}$ ($M_{4b}$). The de-coupling capacitors together with the RLC routing network present an equivalent impedance that is inductive but its real part adds to the circuit losses. Therefore, unless the return current path happens to resonate at the same oscillation frequency (through the equivalent inductances and decoupling capacitors along it), the CM oscillation shifts down from the expected value, which is precisely what we observe in our measurements. The DM oscillation frequency is not affected; therefore, the expected TR is decreased. Furthermore, the losses in the return path are added to the losses of the primary inductor, thus degrading the quality factor of the tank. The long return path causes the losses to be comparable to the inductor's loss and this jeopardizes the CM start-up. Furthermore, this path also partially cancels the magnetic field of the inductor, thus degrading its Q-factor. The severe PN degradation compared to the simulation results gives, thus, credence to the Q degradation of the tank.

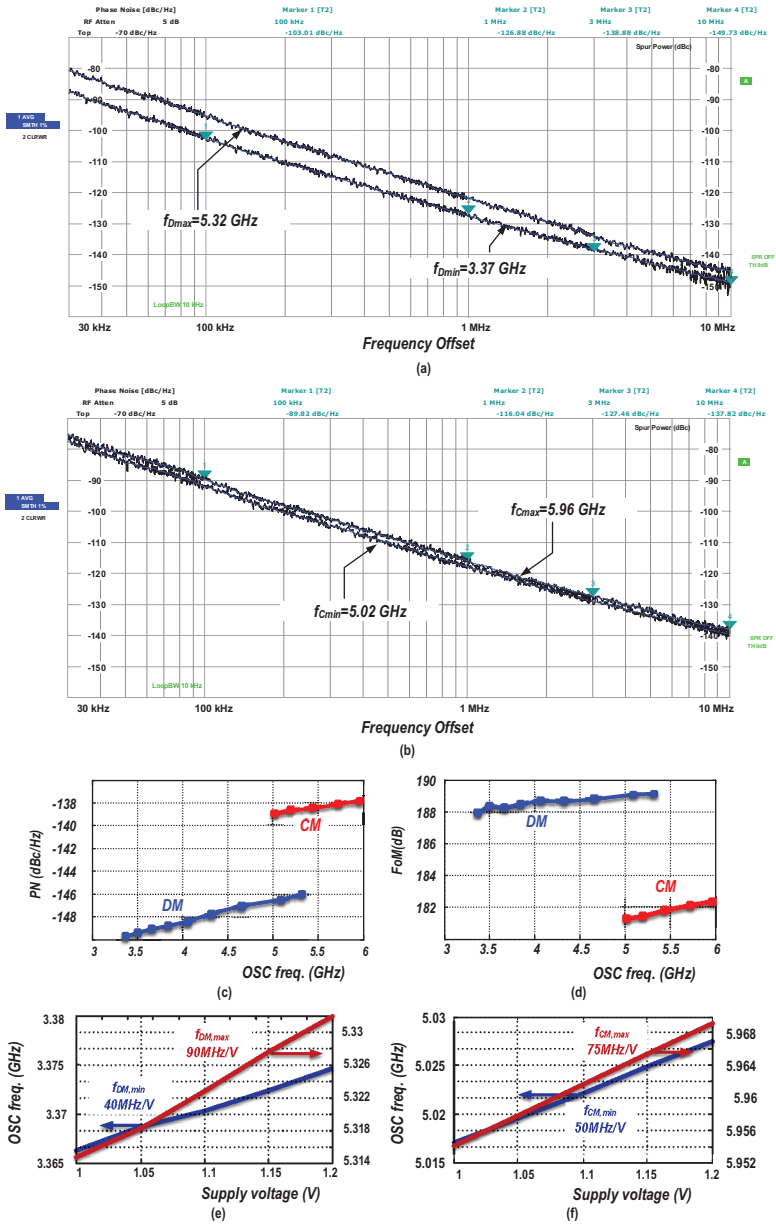


**Figure 7.19** (a) Measured PN at $f_{DM,max}$, $f_{DM,min}$; (b) $f_{CM,max}$ and $f_{CM,min}$. Measured (c) PN and (d) FoM at 10-MHz offset across TR. Frequency pushing due to supply voltage variation in (e) DM and (f) CM oscillators.

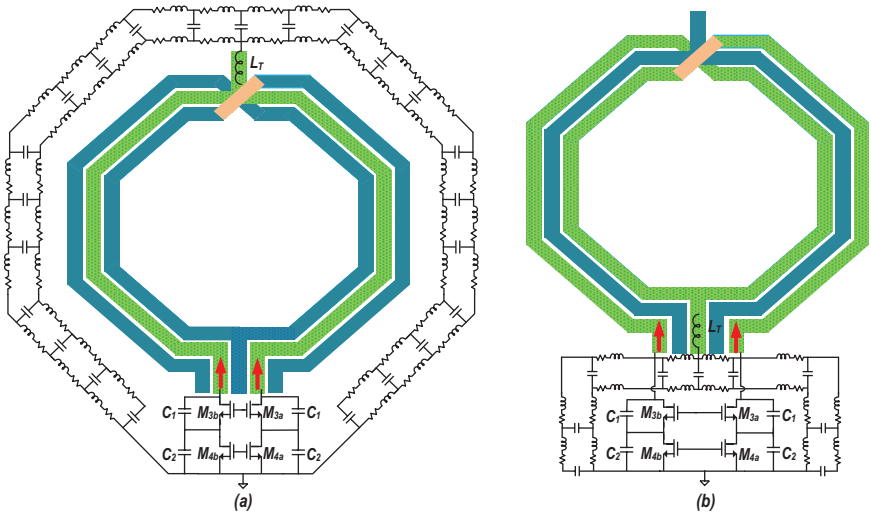


**Figure 7.20** Return current path in the 1:2 transformer.

Our EM simulations predict a 0.25-Ω resistance in this path and circuit simulations show that such resistance in series with the primary inductor would degrade the CM oscillator phase noise by 4 dB. This appears to agree with our measurements.

One possible solution would be employing a 2:1 transformer. A 2-turn primary inductor will have its supply connection node very close to the transistors; therefore, the current return path would not be very long, thus minimizing the path inductance. However, in that transformer, the CM current in the two windings of the primary inductor has opposite direction, thus canceling each other's flux [30]. Consequently, the CM primary inductance would be smaller than the DM one. The spacing between the transformer windings should be chosen properly to satisfy the overlap condition for the reasonable capacitor bank $C_{\text{on}}/C_{\text{off}}$ ratios.

## 7.6 Conclusion

In this chapter, we have introduced a technique to extend a tuning range (TR) of an LC-tank oscillator without significantly increasing its die area. A strongly coupled 1:2 turns-ratio transformer-based tank is normally excited in a differential mode (DM), where it achieves the TR of 45% with a good FoM of 188.2–189.4 dB. The TR is extended by exciting the tank in

common mode (CM) with two locked Colpitts oscillators. This oscillator is implemented in 40 nm CMOS and delivers the total TR of 55.5% while constraining the core die area to only 0.12 $mm^2$. Although the measured tuning range extension and phase noise (PN) in the CM mode were worse than theoretically predicted, we have identified the common cause as a current return route inductance that not only lowers the CM frequencies but also adds losses that result in a reduced Q-factor.

## References

[1] M. Carusol, M. Bassi, A. Bevilacqua, and A. Neviani, "Wideband 2–16GHz local oscillator generation for short-range radar applications," *in Proc. of the IEEE European Solid-State Circuits Conference(ESSCIRC)*, 2012, pp. 353–356.

[2] J. Borremans et al., "A 86 MHz–12 GHz digital-intensive PLL for software-defined radios, using a 6 fJ/step TDC in 40 nm digital CMOS" *IEEE J. Solid-State Circuits*, vol. 45, no. 10, pp. 2116–2129, Oct. 2010.

[3] Y. Chen, Y. Pei, and D. M. W. Leenaerts, "A dual-band LO generation system using a 40GHz VCO with a phase noise of 106.8dBc/Hz at 1-MHz," *in IEEE Radio Frequency Integrated Circuits Symposium (RFIC)*, 2013, pp. 203–206.

[4] L. Fanori, T. Mattsson, and P. Andreani, "A 2.4-to-5.3 GHz dual core CMOS VCO with concentric 8-shape coils," *in IEEE Int. Solid-State Circuits Conf. Dig Tech. Papers (ISSCC)*, Feb. 2014, pp. 370–372.

[5] Z. Safarian, and H. Hashemi, "Wideband multi-mode CMOS VCO design using coupled inductors," *IEEE Trans. Circuits Syst. I, Reg. Papers*, vol. 56, no. 8, pp. 1830–1843, Aug. 2007.

[6] S.-M. Yim and K. O. Kenneth, "Demonstration of a switched resonator concept in a dual-band monolithic CMOS LC-tuned VCO," *in Proc. IEEE Custom Integr. Circuits Conf.*, 2001, pp. 205–208.

[7] N. D. Dalt, E. Thaller, P. Gregorius, and L. Gazsi, "A compact triple-band low-jitter digital LC PLL with programmable coil in 130 nm CMOS," *IEEE J. Solid-State Circuits*, vol. 40, no. 7, pp. 1482–1490, Jul. 2005.

[8] Z. Li and K. S. O, "A low-phase-noise and low-power multiband CMOS voltage-controlled oscillator," *IEEE J. Solid-State Circuits*, vol. 40, no. 6, pp. 1296–1302, Jun. 2005.

[9] D. Hauspie, E. Park, and J. Craninckx, "Wideband VCO with simultaneous switching of frequency band, active core, and varactor size," *IEEE J. Solid-State Circuits*, vol. 42, no. 7, pp. 1472–1480, Jul. 2007.

[10] N. T. Tchamov, S. S. Broussev, I. S. Uzunov, and K. K. Rantala, "Dual band LC VCO architecture with a fourth-order resonator," *IEEE Trans. Circuits Syst. II, Exp. Briefs*, vol. 54, no. 3, pp. 277–281, Mar. 2007.

[11] A. Buonomo and A. Lo Schiavog, "Analysis and design of dual-mode CMOS LC-VCOs," IEEE Trans. Circuits Syst. I, Reg. Papers, vol. 62, no. 7, pp. 1845–1853, Nov. 2015.

[12] A. Italia, C. Marco Ippolito, and G. Palmisano, "A 1-mW 1.13–1.9 GHz CMOS LC VCO using shunt-connected switched-coupled inductors," IEEE Trans. Circuits Syst. I, Reg. Papers, vol. 59, no. 6, pp. 1145–1155, Jun. 2012.

[13] B. Sadhu, J. Kim, and R. Harjani, "A CMOS 3.3-8.4 GHz wide tuning range, low phase noise LC VCO," *IEEE Custom Integrated Circuits Conf. (CICC)*, Sep. 2009.

[14] W. Deng, K. Okada, A Matsuzawa, "A 25MHz–6.44GHz LC-VCO using a 5-port inductor for multi-band frequency generation," *IEEE Radio Frequency IC Symposium*, Jun. 2011, pp. 1–4.

[15] S. Rong and H. C. Luong "Analysis and design of transformer-based dual-band VCO for software-defined radios," *IEEE Trans. on Microwave Theory and Techniques*, vol. 59, no. 3, pp. 449–462, Mar. 2012.

[16] A. El-Gouhary, N. M. Neihart, An analysis of phase noise in transformer-based dual-tank oscillators," *IEEE Trans. on Microwave Theory and Techniques*, vol. 61, no. 7, pp. 2098–2109, Jul. 2014.

[17] J. Yin and H. C. Luong, "A 57.5–90.1-GHz magnetically tuned multimode CMOS VCO," *IEEE J. Solid-State Circuits*, vol. 48, no. 8, pp. 1851–1861, Aug. 2013.

[18] U. Decanis, A. Ghilioni, E. Monaco, A. Mazzanti, and F. Svelto, "A low-noise quadrature VCO based on magnetically coupled resonators and a wideband frequency divider at millimeter waves," *IEEE J. Solid-State Circuits*, vol. 46, no. 12, pp. 2943–2955, Dec. 2011.

[19] G. Li and E. Afshari, "A distributed dual-band LC oscillator based on mode switching," *IEEE Trans. on Microwave Theory and Techniques*, vol. 59, no. 1, pp. 99–107, Jan. 2011.

[20] G. Li, Y. Tang, and E. Afshari, "A low phase-noise wide tuning-range oscillator based on resonant mode switching," *IEEE J. Solid-State Circuits*, vol. 47, no. 6, pp. 1295–1308, Jun. 2012.

[21] M. Taghivand, K. Aggarwal, and A. S. Y. Poon, "A 3.24-to-8.45 GHz low-phase-noise mode-switching oscillator," *in IEEE Int. Solid-State Circuits Conf. Dig Tech. Papers (ISSCC)*, Feb. 2014, pp. 368–370.

[22] F.-W. Kuo, R. Chen, K. Yen, H.-Y. Liao, C.-P. Jou, F.-L. Hsueh, M. Babaie, and R. B. Staszewski, "A 12mW all-digital PLL based on class-F DCO for 4G phones in 28nm CMOS," *Proc. of IEEE Symp. on VLSI Circuits (VLSI)*, sec. 9.4, pp. 1–2, June 2014.

[23] M. Babaie and R. B. Staszewski, "An ultra-low phase noise class-$F_2$ CMOS oscillator with 191dBc/Hz FOM and long term reliability," *IEEE J. Solid-State Circuits*, vol. 50, no. 3, pp. 679–692, Mar. 2015.

[24] M. Babaie and R. B. Staszewski, "A class-F CMOS oscillator," *IEEE J. Solid-State Circuits*, vol. 48, no. 12, pp. 3120–3133, Dec. 2013.

[25] A. Bevilacqua, F. P. Pavan, C. Sandner, A. Gerosa, and A. Neviani, "Transformer-based dual-mode voltage-controlled oscillators," *IEEE Trans. Circuits Syst. II, Exp. Briefs*, vol. 54, no. 4, pp. 293–297, Apr. 2007.

[26] A. Mazzanti and A. Bevilacqua, "On the Phase Noise Performance of Transformer-Based CMOS Differential-Pair Harmonic Oscillators," *IEEE Trans. Circuits Syst. I, Reg. Papers*, vol. 62, no. 9, pp. 293–297, Sep. 2015.

[27] P. Andreani et al., "A study of phase noise in Colpitts and LC-tank CMOS oscillators," *IEEE J. Solid-State Circuits*, vol. 40, no. 5, pp. 1107–1118, May 2005.

[28] A. Hajimiri and T. H. Lee, "A general theory of phase noise in electrical oscillators," *IEEE J. Solid-State Circuits*, vol. 33, no. 2, pp. 179–194, Feb. 1998.

[29] D. Murphy, J. J. Rael, and A. A. Abidi "Phase noise in LC oscillators: A phasor-based analysis of a general result and of loaded Q," *IEEE Trans. Circuits Syst. I, Reg. Papers*, vol. 57, no. 6, pp. 1187–1203, June 2010.

[30] D. Chowdhury, L. Ye, E. Alon, and A. M. Niknejad, "An efficient mixed-signal 2.4-GHz polar power amplifier in 65-nm CMOS technology," *IEEE J. Solid-State Circuits*, vol. 46, no. 8, pp. 1796–1809, Aug. 2011.

[31] B. Soltanian and P. Kinget, "A low phase noise quadrature LC VCO using capacitive common-source coupling," in *IEEE European Solid-State Circuits Conference (ESSCIRC)*, 2006, pp. 436–439.

[32] Y. Wu, M. Shahmohammadi, Y. Chen, P. Lu, and R. B. Staszewski, "A 3.5–6.8-GHz wide-bandwidth DTC-assisted fractional-N all-digital PLL with a MASH $\Delta\Sigma$-TDC for low in-band phase noise," *IEEE Journal of Solid-State Circuits (JSSC)*, vol. 52, no. 7, pp. 1885–1903, Jul. 2017.

[33] M. Shahmohammadi, M. Babaie, and R. B. Staszewski, "Tuning range extension of a transformer-based oscillator through common-mode Colpitts resonance," *IEEE Trans. on Circuits and Systems I (TCAS-I)*, vol. 64, no. 4, pp. 836–846, Apr. 2017.

[34] M. Shahmohammadi, M. Babaie, and R. B. Staszewski, "Radio frequency oscillator," *US Patent 2017/0324378*, published 9 Nov. 2017.